



**HAL**  
open science

## Mineralization kinetics of biosiliceous sediments in hot subseafloors

Ivano Aiello, Tobias Höfig, Armelle Riboulleau, Andreas Teske, Daniel Lizarralde, Jeanine Ash, Diana Bojanova, Martine Buatier, Virginia Edgcomb, Christophe Galerne, et al.

### ► To cite this version:

Ivano Aiello, Tobias Höfig, Armelle Riboulleau, Andreas Teske, Daniel Lizarralde, et al.. Mineralization kinetics of biosiliceous sediments in hot subseafloors. *Geochimica et Cosmochimica Acta*, 2024, 380, pp.71-82. 10.1016/j.gca.2024.07.005 . hal-04680163

HAL Id: hal-04680163

<https://hal.science/hal-04680163v1>

Submitted on 30 Aug 2024

**HAL** is a multi-disciplinary open access archive for the deposit and dissemination of scientific research documents, whether they are published or not. The documents may come from teaching and research institutions in France or abroad, or from public or private research centers.

L'archive ouverte pluridisciplinaire **HAL**, est destinée au dépôt et à la diffusion de documents scientifiques de niveau recherche, publiés ou non, émanant des établissements d'enseignement et de recherche français ou étrangers, des laboratoires publics ou privés.



Distributed under a Creative Commons Attribution - NonCommercial 4.0 International License



Contents lists available at [ScienceDirect](https://www.sciencedirect.com)

# Geochimica et Cosmochimica Acta

journal homepage: [www.elsevier.com/locate/gca](http://www.elsevier.com/locate/gca)



## Mineralization kinetics of biosiliceous sediments in hot subseafloors

Ivano W. Aiello<sup>a,\*</sup>, Tobias W. Höfig<sup>b,ad</sup>, Armelle Riboulleau<sup>c</sup>, Andreas P. Teske<sup>d</sup>, Daniel Lizarralde<sup>e</sup>, Jeanine L. Ash<sup>f</sup>, Diana P. Bojanova<sup>g</sup>, Martine D. Buatier<sup>h</sup>, Virginia P. Edgcomb<sup>e</sup>, Christophe Y. Galerne<sup>j</sup>, Swanne Gontharet<sup>i</sup>, Verena B. Heuer<sup>j</sup>, Shijun Jiang<sup>k</sup>, Myriam A.C. Kars<sup>b,l</sup>, Ji-Hoon Kim<sup>m</sup>, Louise M.T. Koornneef<sup>n</sup>, Kathleen M. Marsaglia<sup>o</sup>, Nicolette R. Meyer<sup>p</sup>, Yuki Morono<sup>q</sup>, Raquel Negrete-Aranda<sup>r</sup>, Florian Neumann<sup>ac</sup>, Lucie C. Pastor<sup>s</sup>, Manet E. Peña-Salinas<sup>t</sup>, Ligia L. Pérez-Cruz<sup>u</sup>, Lihua Ran<sup>v</sup>, John A. Sarao<sup>w</sup>, Florian Schubert<sup>x</sup>, S. Khogenkumar Singh<sup>y</sup>, Joann M. Stock<sup>z</sup>, Laurent Toffin<sup>s</sup>, Wei Xie<sup>k</sup>, Toshiro Yamanaka<sup>aa</sup>, Guangchao Zhuang<sup>ab</sup>

<sup>a</sup> San Jose State University, Moss Landing Marine Laboratories, Moss Landing, CA 95039, USA

<sup>b</sup> International Ocean Discovery Program, Texas A&M University, College Station, TX 77845, USA

<sup>c</sup> Laboratoire d'Océanologie et de Géosciences, UMR 8187, Université de Lille, CNRS, Villeneuve d'Ascq 59655, France

<sup>d</sup> Department of Earth, Marine and Environmental Sciences, University of North Carolina at Chapel Hill, Chapel Hill, NC 27599, USA

<sup>e</sup> Department of Geology and Geophysics, Woods Hole Oceanographic Institution, Woods Hole, MA 02543, USA

<sup>f</sup> Department of Earth, Environmental and Planetary Sciences, Rice University, Houston, TX 77005, USA

<sup>g</sup> Department of Earth Sciences, University of Southern California, Los Angeles, CA 90089, USA

<sup>h</sup> Chrono-Environnement, UMR 6249-CNRS, Université Bourgogne Franche-Comté, Besançon 25030, France

<sup>i</sup> LOCEAN UMR 7159 Sorbonne Université/CNRS/IRD/MNHN, 4 place Jussieu – boîte 100, F-75252 Paris, France

<sup>j</sup> MARUM – Center for Marine Environmental Sciences, University of Bremen, Bremen, Germany

<sup>k</sup> College of Oceanography, Hohai University, Nanjing, China

<sup>l</sup> Center for Advanced Marine Core Research, Kochi University, Nankoku-shi 783-8502, Japan

<sup>m</sup> Marine Geology & Energy Division, Korea Institute of Geoscience & Mineral Resources (KIGAM), Daejeon 305-350, Republic of Korea

<sup>n</sup> Earth and Environmental Sciences, School of Geography, University of Plymouth, Plymouth, Devon PL4 8AA, United Kingdom

<sup>o</sup> Department of Geological Sciences, California State University, Northridge, CA 91330-8266, USA

<sup>p</sup> Department of Earth System Science, Stanford University, Stanford, CA 94305, USA

<sup>q</sup> Kochi Institute for Core Sample Research, Institute for Extra-cutting-edge Science and Technology Avant-garde Research (X-star), Japan Agency for Marine-Earth Science and Technology, Nankoku Kochi 783-8502, Japan

<sup>r</sup> Investigador por Mexico, Department of Geology, CICESE, Ensenada, BC 22860, Mexico

<sup>s</sup> IFREMER, Centre de Brest, 29280 Plouzané, France

<sup>t</sup> Department of Coastal Oceanography, UABC, Zona Playitas, Ensenada, BC 22860, Mexico

<sup>u</sup> Institute of Geophysics, Universidad Nacional Autónoma de México (UNAM), Mexico City 04510, Mexico

<sup>v</sup> The Second Institute of Oceanography, Ministry of Natural Resources, Laboratory of Marine Ecosystem and Biogeochemistry, Hangzhou, China

<sup>w</sup> College of Geosciences, Texas A&M University, College Station, TX 77843, USA

<sup>x</sup> Section Geomicrobiology, GFZ German Research Centre for Geosciences, Telegrafenberg, 14473 Potsdam, Germany

<sup>y</sup> Department of Geological Oceanography, CSIR - National Institute of Oceanography, Goa 403004, India

<sup>z</sup> Division of Geological and Planetary Sciences, California Institute of Technology, Pasadena, CA 91125, USA

<sup>aa</sup> Department of Ocean and Environmental Sciences, Tokyo University of Marine Science and Technology, Tokyo, 108-8477, Japan

<sup>ab</sup> Laboratory for Marine Ecology and Environmental Science, Qingdao National Laboratory for Marine Science and Technology, Qingdao, 266237, China

<sup>ac</sup> GFZ, German Research Centre for Geosciences, Section 4.8 Geoenergy, Telegrafenberg, 14473 Potsdam, Germany

<sup>ad</sup> Present address: Project Management Jülich, Research Centre Jülich, Schweriner Str. 44, 18069 Rostock, Germany

### ARTICLE INFO

Associate editor: Benjamin Tutolo

### Keywords:

Silica diagenesis

### ABSTRACT

Temperature affects the timing of the transformation of amorphous silica (opal-A) into crystalline (opal-CT) exponentially. Thus, in hot subseafloor environments opal-A is expected to convert into opal-CT at relatively shallow burial depths, where *in situ* temperatures do not exceed ~56 °C, as it has been previously observed at various deep-sea sites and in onshore rock outcrops as well as assessed during lab experiments. The response of

\* Corresponding author.

E-mail address: [ivano.aiello@sjsu.edu](mailto:ivano.aiello@sjsu.edu) (I.W. Aiello).

<https://doi.org/10.1016/j.gca.2024.07.005>

Received 26 December 2023; Accepted 5 July 2024

Available online 14 July 2024

0016-7037/© 2024 The Author(s). Published by Elsevier Ltd. This is an open access article under the CC BY-NC license (<http://creativecommons.org/licenses/by-nc/4.0/>).

Mineralization kinetics  
opal-A  
opal-CT  
IODP Expedition 385  
Paleothermometry

biosilica (biogenic opal-A) diagenesis to steep geothermal gradients (~224–529 °C/km) at extremely high sedimentation rates (~1 m/kyr) was examined in cores from off-axis boreholes drilled by the International Ocean Discovery Program (IODP) Expedition 385 in the actively spreading, intrusive sill-riddled Guaymas Basin at the Gulf of California (Mexico) rifted margin. At three sites drilled by IODP Expedition 385 (U1545, U1546, and U1547), the conversion from amorphous opal (–A) to crystalline opal (–CT) occurs in relatively deep (up to ~330 mbsf) and unexpectedly hot (*in situ* temperatures of ~74–79 °C) seafloor conditions. This observation indicates a significantly slower reaction kinetics of biosilica transformation than previously reported. A compilation of empirical data that include biosiliceous basins with a similarly hot seafloor (Sea of Japan and Bering Sea) yield new kinetic parameters that account for the slower rates of silica transformation. Thus, current kinetic models for the prediction of opal-A to –CT conversion face limitations when burial rates exceed those typical of biogenic sedimentation in open-ocean conditions. At Guaymas Basin Site U1545, where there is no evidence of sill-related metamorphic overprint, the d-spacing of the opal-CT (101) peak correlates linearly with *in situ* temperature between ~75 and 110 °C throughout the opal-CT zone, thus, providing a local silica paleothermometry proxy that can be used to calculate the maximum temperature to which opal-CT sediment has been subjected.

## 1. Introduction

Biosiliceous sediments and sedimentary rocks have played a prominent role in the marine geological record throughout the Phanerozoic. However, silica exoskeletons usually dissolve in the present-day oceans as they sink in the water column (e.g., Tréguer and De La Rocha, 2013). Thus, the preservation of abundant biosilica in Jurassic to Quaternary sediments is mainly related to areas of upwelling and high primary productivity that rapidly deposit biogenic silica (Heath, 1974; Hein and Karl, 1983). Generally, this oceanographic setting is spatially and temporally associated with tectonically controlled marginal/young ocean basins. For instance, the Western Tethys radiolarite deposits represent a Jurassic belt of bedded cherts associated with rifted continental margin and ophiolite units across southern and central Europe (Folk and McBride, 1978). In western North America, the Miocene Monterey Formation of California (USA) formed by extremely thick accumulations of diatom ooze that may have recorded the onset of a high-productivity regime along a proto-California Current system (Pisciotta and Garrison, 1981). Biosilica sedimentation of the Monterey Formation occurred in a tectonic setting characterized by steep-sided pull-apart basins separated by submarine banks or emergent islands (Ingle, 1981). The resulting rugged seafloor morphology could have enhanced water mass mixing and primary productivity through upwelling along morphological obstructions that also reduced input of terrigenous sediment. These oceanographic and tectonic conditions are comparable to the modern Gulf of California, one of the world's most productive upwelling regions well known for the deposition and burial of diatomaceous ooze (Baumgartner et al., 1985; Thunell et al., 1993; Douglas et al., 2007).

Massive deposits of siliceous plankton are important not only because of their distinct paleoceanographic setting as high-resolution paleoenvironmental archive but also because their extremely porous and water-rich opaline tests (up to 14 wt%; Hesse and Schacht, 2011) experience profound alteration as the material undergoes diagenesis with increasing burial. This process leads to dramatic changes in physical and chemical properties mainly because of the successive mineralogic transformations of biogenic amorphous silica (opal-A) into quartz (Jones and Segnit, 1971), arguably being one of the most significant early diagenetic processes in marine sediments. Commonly, authigenic quartz does not form directly from opal-A dissolution and following silica reprecipitation but is preceded by precipitation of the metastable silica phases opal-A' (X-ray amorphous like opal-A) and/or opal-CT (mixture of non-crystalline structure and “disordered”  $\alpha$ -cristobalite and –tridymite; Jones and Segnit, 1971; Hein et al., 1978; Kastner et al., 1977; Riech and von Rad, 1979; Williams et al., 1985). But there are exceptions: quartz can form at low temperature (e.g., Lancelot, 1973; Ocean Drilling Program (ODP) Site 1226: Meister et al., 2014). Nevertheless, rates of transformation among silica polymorphs are slow enough in the shallow crust so that metastable polymorphs may persist

once precipitated (Williams and Crerar, 1985). In comparison to opal-A, the solubility of opal-CT and quartz is lower by one and two orders of magnitude, respectively, with each of these diagenetic steps involving dissolution of a less ordered silica polymorph in favor of precipitation of a more ordered form (Kastner, 1981). The opal-A to quartz transformation follows a diagenetic dissolution-reprecipitation pathway which is controlled mainly by the aqueous solubility of the phases, in turn being a function of crystal structure, particle size and shape, pH of the water, temperature and to a much lesser extent pressure, type and concentration of other dissolved silica species, accompanying minerals in the sediment, and pore-water diffusion rates (Williams et al., 1985). The irreversible conversion from opal-A to opal-CT corresponds to marked changes in physical properties. This process includes both a dramatic drop in porosity (Isaacs, 1981; Chaika and Dvorkin, 2000) and fundamental changes in rheology, with opal-CT sediments being harder, more brittle, and more prone to fracturing than those made up of opal-A. In turn, fractures may increase permeability and promote lateral or up-dip flow of fluids (Gross, 1995; Aiello et al., 2001). The transition to opal-CT is manifested as a distinct reflector in seismic reflection profiles of biosiliceous sediment successions (e.g., Kuramoto et al., 1992), and this transition can cause kilometer-scale differential compaction and subsidence as well as the expulsion of pore fluids (Davies et al., 2008).

Temperature affects the timing of opal-CT precipitation exponentially as demonstrated by Mizutani (1970). The kinetic models derived from silica precipitation experiments in an alkaline solution at hydrothermal temperatures of ~100–300 °C show that opal-CT forms ten times faster (~4 d instead of ~40 d) when the temperature increases by ~60 °C (from ~104 to ~162 °C; Mizutani, 1970). In natural systems, the temperatures reported for the transition between the silica polymorphs cover relatively broad and partially overlapping ranges of ~18–56 °C for opal-A to opal-CT and ~30–110 °C for opal-CT to quartz (Murata and Larson, 1975; Iijima and Tada, 1981; Keller and Isaacs, 1985; Hesse and Schacht, 2011, and references therein). The comprehensive analysis of Deep Sea Drilling Project (DSDP) data by Pisciotta (1981) shows that (1) much of the biogenic opal deposited during the Neogene has not been converted into opal-CT yet, (2) the precipitation of opal-CT in marine sediments commonly falls within the limited time and temperature fields predicted by kinetic models (e.g., Mizutani, 1970), and (3) the rates of silica transformations are relatively high (i.e., a few millions versus tens of millions of years) if the thermal gradient and the sedimentation rates are high.

High sedimentation rates coupled with large thermal gradients are conditions typical of nascent, upwelling basins such as the Gulf of California (Fig. 1a), which hosts young (<6 Ma), active oceanic spreading centers (Lizarralde et al., 2007) as well as rapid sedimentation of mainly diatomaceous ooze (Calvert, 1966). Based on DSDP Leg 64 (1978/79) sediment cores recovered from the gulf's central spreading segments in the Guaymas Basin, the formation of authigenic silica took only tens of thousands of years upon onset of burial, making these biosilica deposits

the youngest known to be transformed into opal-CT (Kastner and Siever, 1983). In the Guaymas Basin, the early onset of silica phase change has been attributed to thermal impact from sills that intruded the sediment successions in or proximal to the two axial troughs (Fig. 1b; Kastner and Siever, 1983), which were interpreted as the only loci of magmatism in this nascent ocean basin (Einsle et al., 1980). More recently, basin-wide seismic imaging has indicated, however, that magmatism extends beyond the troughs so that the subseafloor sedimentary fill is riddled with shallow igneous intrusions over several tens of kilometers from the spreading axis (Lizarralde et al., 2011). International Ocean Discovery Program Expedition 385 (IODP X385) extended the deep-sea drilling of the basin's subseafloor to parts offset up to ~50 km relative to the axial graben of the northern Guaymas Basin spreading segment (Table 1; Fig. 1b). Two adjacent drill sites (Sites U1545 and U1546) recovered the same biosiliceous sedimentary setting unaffected by magmatism (U1545) and disturbed by a massive sill (U1546), respectively, and a third location (Site U1547) was selected to investigate a shallow sill associated with present-day hydrothermal activity at the seafloor (Teske et al., 2019, 2021; Cheviet et al., 2023; Neumann et al., 2023). The interpretation of seismic stratigraphic data constrains the time of the sill

intrusion at Site U1546 between 76 ka and 149 ka (Lizarralde et al., 2023). Modern drilling technology, including advanced hydraulic piston coring, has enabled high and continuous core recovery of sediments as well as the collection of high-resolution downhole porewater geochemistry data and *in situ* temperature measurements in the Guaymas Basin providing for more detailed examination and understanding of biosilica diagenesis at high temperatures.

## 2. Materials and methods

### 2.1. Study sites

While R/V *JOIDES Resolution* drilled eight sites during IODP X385 in the Guaymas Basin, Gulf of California, this study focuses on Sites U1545, U1546, and U1547 (Fig. 1B) which are the off-axis sites where the opal-A to opal-CT transition zone was recovered. Each site was drilled multiple times, with holes at a site being at a maximum distance of ~50 m from each other. Most of the samples and the physical properties data used in this paper come from the first hole drilled (Hole A) at each site although they have been integrated with samples and data from other

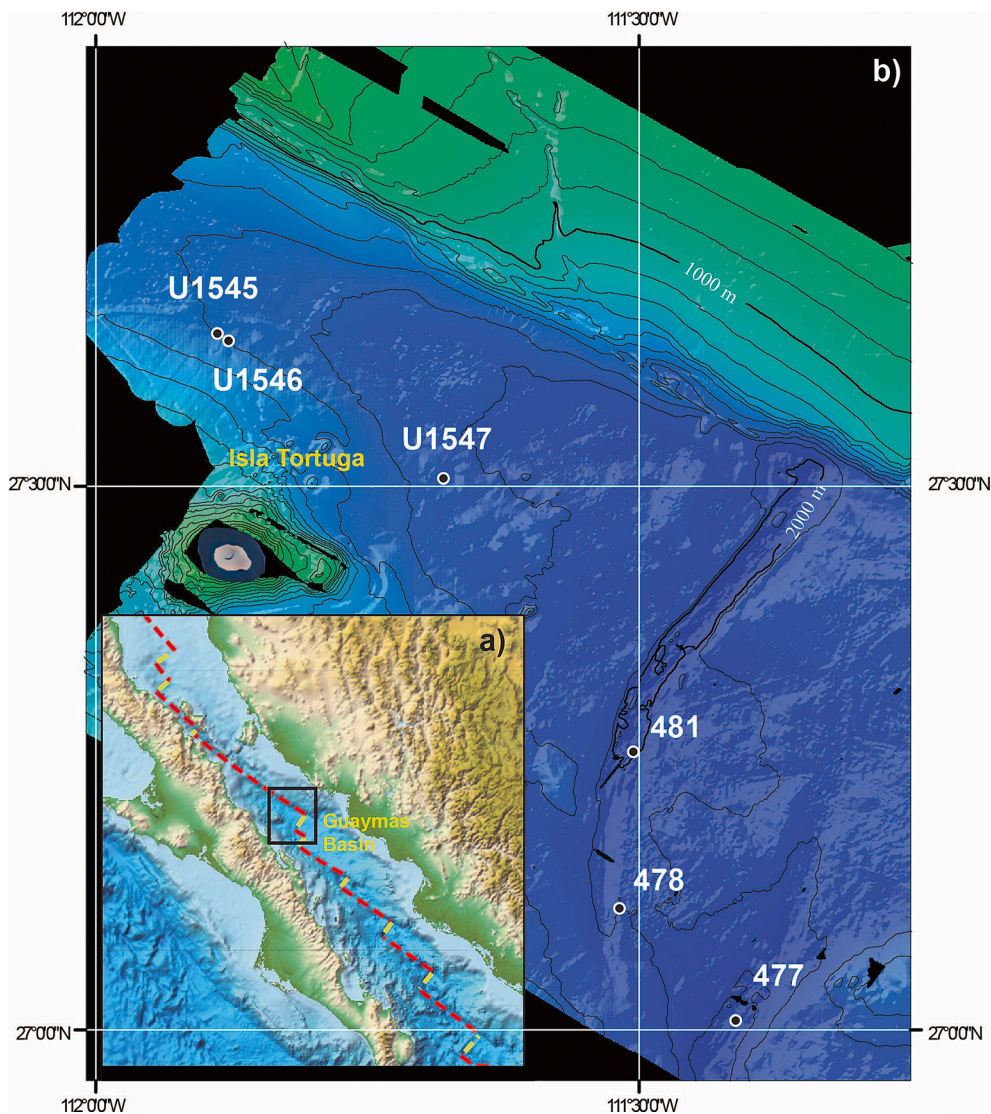


**Fig. 1.** (a) Bathymetric map of the Gulf of California with the box inset identifying the location of the Guaymas Basin (Fig. 1b). The yellow dashed lines indicate the location of the spreading segments, the red dashed lines represent the transform faults. (b) Bathymetric map of the Guaymas Basin showing the locations of DSDP Leg 64 Sites 477, 478, and 481 at or near axial troughs (graben) that mark the basin's spreading segments and the off-axis IODP X385 drill Sites U1545, U1546, and U1547 located northwest of the spreading area and just north of Isla Tortuga.

**Table 1**

Summary of IODP Expedition 385 drill sites presented in this study. mbsf = meters below sea floor.

Site‡	Total penetration (m)	Geothermal gradient (°C/km)	Sedimentation rate (cm/k. y.)+	Shallowestopal-CT (mbsf)	Total thickness opal-CT zone (m)	Temperature opal-A/CT transition (°C)
U1545	503.3	225	86.3	329	121	79
U1546	540.1	221	102	325	173 ◇◇	74
U1547	209.8*	529	52.4**	127	24	77

Notes: ‡Sites coordinates (lat., long., water depth): Site U1545 (27°38.2325'N, 111°53.3406'W, 1593 m), Site U1546 (27°37.8851'N, 111°52.7939'W, 1586 m), Site U1547 (27°30.4561'N, 111°40.6980'W, 1733 m); +Based on X385 shipboard biostratigraphy (Teske et al., 2021a); \*Maximum penetration was obtained at Hole B; \*\*Minimum age estimate because of lack of biomarkers; ◇◇ Includes intervening sill and authigenic quartz in contact zone (between ~333 mbsf – 447 mbsf).

holes as well if necessary/possible.

The lithologic record at these sites comprises middle to late Pleistocene sediments that are primarily laminated diatom ooze and secondarily terrigenous mud (mainly clay minerals) with subordinate calcareous nannofossils, siliciclastic silt, and authigenic minerals (Teske et al., 2021). The latter mainly consist of dolomite that occurs in the form of both disseminated micrite particles and discrete concretions with different degrees of lithification. The interval of intrusive igneous rocks cored at Sites U1546 and U1547 is more than 50 m thick, but only ~0.9 m thick at Site U1545. The depth at which the main silica phase changes from opal-A to opal-CT was approximately identified at each of the three IODP X385 sites based on a major lithologic transition from softer diatom ooze to more brittle porcelanite (Teske et al., 2021). The mineralogic analysis of the samples analyzed for this study has further constrained the depth at which this transition occurs as well as determined the thicknesses of the sediments in which opal-CT is the main silica phase (the “opal-CT zone”; Table 1).

## 2.2. Shipboard data

Porewater silica concentrations were obtained immediately after core retrieval, from 5–20 cm long whole-round core subsamples that were scraped with a spatula to remove contamination from seawater and sediment smearing. Subsequently, porewater was collected by compressing the whole-round core samples in a titanium squeezer using a laboratory hydraulic press. The porewater was analyzed on board for major and minor elements, including Na<sup>+</sup>, Ca<sup>2+</sup>, Mg<sup>2+</sup>, K<sup>+</sup>, Li<sup>+</sup>, B, Si, Ba<sup>2+</sup>, Fe, Mn, and Sr<sup>2+</sup>, using an Agilent 5110 inductively coupled plasma–optical emission spectrometer (ICP-OES) with an SPS4 autosampler. The instrument was run in an ICP atomic emission spectrometry (AES) elemental analysis mode following published inorganic geochemistry analysis protocols, being detailed by the IODP X385 methods (Teske et al., 2021, and references therein). Table S1 reports silica concentrations (in μM) for IODP X385 Sites U1545, U1546, and U1547.

*In situ* temperature measurements in undisturbed sediment successions were carried out using the advanced piston corer temperature (APCT-3) tool and the Sediment Temperature 2 (SET2) tool. The latter is used when sediments are too stiff for the former tool to be deployed. Details of the *in situ* temperature acquisition and thermal analysis of IODP X385 can be found in Teske et al. (2021) and Neumann et al. (2023), respectively. The relationship between temperature and depth is significantly linear ( $R^2 = 0.99$ ,  $p = 2.5871 \times 10^{-18}$ , RMSE = 1.84 °C). Table S2 reports *in situ* temperatures for IODP X385 Sites U1545, U1546 and U1547.

## 2.3. X-ray diffraction (XRD)

All mineralogic analyses reported here were performed with a Rigaku SmartLab XRD instrument equipped with a CuKα radiation source ( $\lambda = 1.54060 \text{ \AA}$ ) using a 10 mm slit at a tube voltage of 40 kV and a current of 40 mA. The instrument is controlled by Rigaku's SmartLab Studio II proprietary software. Samples were first dried and crushed in a mortar and then randomly oriented powders were obtained after sieving

at 63 μm. Each measurement was done after vertical alignment between the X-ray source, the surface of the sample and the detector. For all XRD runs,  $2\theta$  ranged between 3°–5° and 65°–90°, scans were done at 1°  $2\theta$  per minute, with a step size of 0.004°  $2\theta$  while the sample was rotating 60 times per minute to insure larger and more homogenous scan areas. All d-spacing measurements reported here are for the main diffraction peak of opal-CT which is the (101) diffraction of  $\alpha$ -cristobalite; the values were rounded to the nearest 3rd digit which is ~1 order of magnitude less than the resolution of the measurement within the interval of interest to study silica diagenesis (the XRD scan of the 21°–22°  $2\theta$  interval with 0.004°  $2\theta$  step size corresponds to a resolution of ~0.0008 Å for  $\lambda = 1.54060 \text{ \AA}$ ; Table 2). Peak search was carried out by Rigaku's SmartLab Studio II software using split-pseudo-Voigt for profile fitting, B-spline for background detection, and the second derivative method was used for automatic peak ID.

The primary silica phase in the Guaymas Basin samples is biogenic silica (opal-A), which is nearly X-ray amorphous and yields a broad bulge between ~4.8 Å and ~3 Å, broadly peaking around ~4 Å (21.7°  $2\theta$ ; Fig. 2A). The degree of crystallization of opal-CT is reflected by the relative position of the most intense (101) peak which results from the overlapping reflections of  $\alpha$ -tridymite and  $\alpha$ -cristobalite (Hein et al., 1978; Herdianita et al., 2000). With increasing mineralogic maturity the peak shifts from ~4.11 Å to ~4.05 Å due to the decrease of d-spacing and the progressive increase in lattice ordering with maturation (Hein et al., 1978; Iijima and Tada, 1981; Kano, 1983; Elzea et al., 1994; Liesegang and Tomaschek, 2020; Fig. 2). The identification of the opal-CT peak was carried out using Rigaku's SmartLab Studio II automatic peak ID option, and further refined manually when it was necessary. The presence of the (200) peak of  $\alpha$ -cristobalite centered at ~36.19°  $2\theta$  (~2.48 Å) with intensity (20) was routinely assessed. The identification of this secondary peak was especially critical to confirm the presence of the (101) peak in the shallowest and least mature samples. The standard deviation for the measurement of opal-CT d-spacing is 0.006 Å as indicated by replicated ( $n = 6$ ) XRD measurements of 4 samples selected from different depths within Site U1545's opal-CT zone (Table S3). This value is ~10 % of the range of d-values for the opal-CT peak (0.06 Å; e.g., Hein et al., 1978; Kano, 1983) and similar to the precision for opal-CT (101) peak measurements by Iijima and Tada (1981). The diffractograms were calibrated using the position of the (101) peak of quartz at ~3.35 Å. The latter is much sharper and consistently identifiable by the automatic peak ID option of the software and has a smaller standard error than the opal-CT (101) peak (Table 2).

## 3. Results

The adjoining Sites U1545 and U1546 (~1 km apart) share not only the same lithologic record of middle to late Pleistocene (<0.44 Ma) sedimentation, largely composed of diatom ooze mixed with clay minerals, but also similar geothermal gradients, porewater silica concentration profiles, and diatom test preservation trends with depth (Fig. 3). The most noticeable lithologic change in the sedimentary succession at both sites is the transition from relatively soft diatom ooze to harder and more brittle biosiliceous rock (porcelanite) starting between ~320 m and ~350 m below seafloor (mbsf). The main difference between the

**Table 2**

Opal-CT (101) and quartz (101) peaks, d-spacing values at Sites U1545, U1546, and U1547.

Site	Sample (Hole/ Core/Section/ Interval)	<i>in situ</i> temperature (T°C)	Depth (mbsf)	Opal-CT (101)d- spacing (Å)	Quartz (101) d- spacing (Å)	
<b>U1545</b>	A_55X_5W_30-35	79.3	328.69	4.106	3.339	
	A_55X_5W_65-75	79.4	328.98	4.096	3.342	
	A_55X_5W_75	79.4	329.09	4.110	3.346	
	A_55X_CC	80.2	332.77	4.108	3.345	
	A_56X_3W_68-69	81.2	336.88	4.104	3.344	
	A_56X_CC	81.8	339.69	4.105	3.358	
	A_58X_CC	84.8	353.02	4.098	3.346	
	A_59X_CC	87.0	362.56	4.090	3.345	
	A_60X_1W_76-77	89.3	372.86	4.077	3.335	
	A_62X_1W_135-140	93.9	392.87	4.083	3.349	
	A_62X_2W_35-40	94.03	393.37	4.073	3.346	
	A_62X_2W_75-80	94.1	393.76	4.086	3.345	
	A_62X_3W_40-41	94.3	394.89	4.078	3.338	
	A_63X_4W_67-68	96.9	406.37	4.081	3.341	
	A_65X_3W_96-97	101.1	424.54	4.075	3.341	
	A_65X_5_35-40	101.6	426.98	4.080	3.344	
	A_65X_5W_45-55	101.6	427.08	4.074	3.338	
	A_65X_CC	102.1	429.28	4.063	3.335	
	A_67X_1W_41-42	104.7	440.61	4.067	3.347	
	A_67X_3W_48-88	105.3	443.42	4.073	3.346	
	A_68X_CC	106.9	450.11	4.057	3.345	
	<b>U1546</b>	A_57X_4W_121-123	73.54	316.81	4.108	3.346
		A_58X_1W_100-102	73.92	318.51	4.105	3.346
		A_59X_1W_100-102	74.91	323.01	4.106	3.347
		A_59X_2W_101-103	75.24	324.52	4.099	3.344
		A_59X_3W_101-103	75.57	326.02	4.100	3.343
		A_59X_4W_102-104	75.9	327.51	4.098	3.346
		A_59X_5W_102-104	76.23	329.01	4.097	3.342
A_60X_1W_120-122		76.89	332.01	4.101	3.347	
A_60X_2W_120-122		77.22	333.51	4.101	3.342	
A_60X_3W_121-123		77.55	335.02	4.092	3.347	
A_60X_3W_131-141		77.583	335.15	4.095	3.345	
A_60X_4W_120-122		77.88	336.51	4.094	3.345	
A_60X_5W_119-121		78.21	338.01	4.084	3.349	
A_60X_6W_119-121		78.54	339.51	4.073	3.347	
C_24R_3W_94-114		103.22	451.71	4.072	3.346	
C_26R_2W_93-98		105.27	461.01	4.081	3.348	
C_26R_3W_71-87		105.45	461.83	4.076	3.347	
C_28R_1W_144-149		107.25	470.03	4.079	4.347	
C_28R_1W_144-150		107.25	470.04	4.079	3.345	
C_31R_1W_118-123		110.44	484.53	4.076	3.345	
C_32R_3W_0-4	111.54	489.51	4.070	3.346		
<b>U1547</b>	B_24F_2W_40-60	127.4	68.97	4.102	3.341	
	B_25F_2W_40-60	131.58	71.10	4.095	3.345	
	B_25F_2W_107-117	132.2	71.42	4.101	3.346	
	A_27X_2W_40-42	137	73.87	4.106	3.344	
	B_28F_2W_40-60	146.03	78.47	4.096	3.345	

**Table 2 (continued)**

Site	Sample (Hole/ Core/Section/ Interval)	<i>in situ</i> temperature (T°C)	Depth (mbsf)	Opal-CT (101)d- spacing (Å)	Quartz (101) d- spacing (Å)
	B_28F_2W_82-87	146.38	78.65	4.098	3.345
	B_29F_2W_78-97	151.24	81.13	4.100	3.345

two sites is the presence of a ~75 m-thick, mafic sill with basaltic, doleritic, and gabbroic textures at Site U1546 (between ~355 mbsf and ~430 mbsf) which does not extend laterally to nearby Site U1545 (Fig. 3a; Teske et al., 2021). At the more southerly Site U1547, the dominant lithology also is diatom ooze, although coarser siliciclastic components are more abundant than at Sites U1545 and U1546. Site U1547 is markedly different from the previous two sites in that a hot, recently emplaced mafic sill is present at much shallower depth, and sediment temperature, dissolved silica content in porewater, and diatom test dissolution increase more rapidly with depth. Silica phase change also begins at much shallower depth at Site U1547, with diatom ooze being fully replaced by porcelanite at ~130 mbsf, ~200 m shallower than at the northwestern sites (Fig. 3b).

Changes in the structure of silica phases coincide with shifts in porewater silica concentrations and degree of diatom test preservation at all three IODP X385 sites reported here. The upper ~270 m of sediment at both Site U1545 and Site U1546 are dominated by amorphous silica as evidenced by XRD patterns showing the characteristically broad opal-A hump centered at ~4 Å. Over the 0 to ~270 mbsf interval, the concentration of silica dissolved in porewater increases steadily from ~700 to ~2200 µM due to the intensified dissolution of the metastable biogenic opal-A (i.e., diatom tests) with depth, coinciding with a continuous downhole temperature increase. The *in situ* sediment temperature increases along a linear geothermal gradient of 225 °C/km and 221 °C/km at Sites U1545 and U1546, respectively. For example, at Site U1545, this downhole temperature evolution translates to an increase from ~4 °C near the seafloor to ~72 °C at ~296 mbsf (Fig. 3c). At the latter temperature and depth, opal-A is still the only detectable siliceous phase (Fig. 2a) while the porewater is subject to a drop in the content of dissolved silica, starting at ~270 mbsf (Fig. 3a). The subsequent overall decrease of ~600 µM, from ~2200 µM to ~1600 µM, over a range of ~55 m (Fig. 3a) suggests the onset of authigenic silica precipitation in this interval. Eventually, below the critical depth of ~325 mbsf, which corresponds to an *in situ* temperature of ~78 °C and ~74 °C at Sites U1545 and U1546, respectively, the preservation of diatom tests decreases dramatically and dissolved silica concentrations decline sharply to reach values similar to the shallow subseafloor (~500 µM; Fig. 3a).

At all three sites, there is a gap between the depth at which the dissolved silica concentrations start to plummet and the depth at which opal-CT is first detected: ~43 m for Site U1545, ~32 m for Site U1546, and ~24 m for Site U1547 (Fig. 3). The gap marks the transition between sediments in which opal-A is the only silica phase and sediments that contain ~10 % opal-CT (the detection limit with XRD; Liesegang and Tomaschek; 2020). The latter are characterized by an emerging opal-CT peak in the XRD profile. Its position thus results from a combination of amorphous and paracrystalline material, being preceded by scanning electron microscopy (SEM) evidence of incipient silica recrystallization (e.g., Fig. 2b). We used the combined evidence of changes in XRD patterns and the formation of silica spherules with µm-sized blades which are the typical feature of opal-CT lepispheres to define the depth of the phase transition from opal-A to opal-CT in which both silica polymorphs coexist (Fig. 2c-e and 3). The opal-CT peaks of the shallowest samples are centered at ~21.60° 2θ (~4.108 Å). Gradually, silica recrystallization and ordering become evident by the decreasing d-spacing of opal-CT with depth, advancing downhole within the opal-CT zone (Fig. 3a).

At Sites U1545 and U1546, the total thickness of the opal-CT zone, defined as the interval between the shallowest occurrence of XRD-

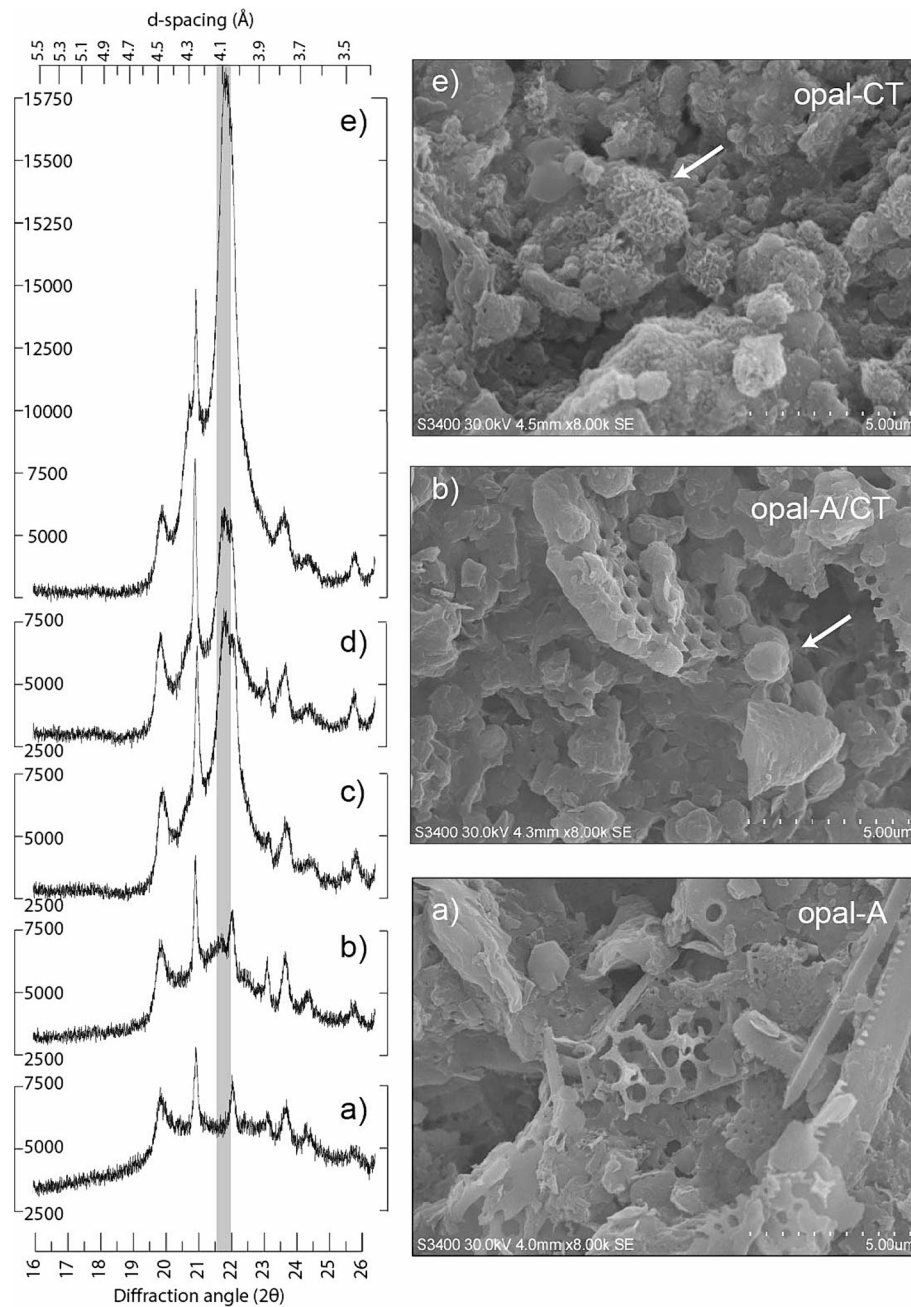


**Fig. 2.** Examples of XRD profiles and selected corresponding scanning electron microscopy (SEM) photomicrographs showing increasing silica recrystallization and diatom dissolution from a) to e). In the SEM close-ups, the magnification for all photographs is 8000 $\times$  and the graduated scale-bar is 5  $\mu\text{m}$ . The samples are all from Site U1545 and shown in the order of increasing depth from bottom to top. (a) Opal-A sample with fragmented diatom tests displaying perfectly preserved fine-structures; Sample U1545A-51F-3 W, 45–50 cm (296.17 mbsf;  $\sim 72^\circ\text{C}$ ); (b) Sample U1545A-55X-5W, 30–35 cm (328.87 mbsf;  $\sim 77^\circ\text{C}$ ) is the shallowest one from Site U1545 that in the SEM image shows evidence of silica precipitation in the form of overgrowth of opal-CT lepispheres (silica spherules  $\sim 1\text{--}2\ \mu\text{m}$  in diameter) on residual fragments of opal-A diatom tests (mostly girdles); (c) Sample U1545A-60X-1 W, 76–77 cm (no corresponding SEM image); (d) Sample U1545A-63X-4 W, 67–68 cm (no corresponding SEM image); (e) Sample U1545A-65X-5W, 45–55 cm, with opal-CT peak at  $\sim 21.8^\circ\ 2\theta$  (427.08 mbsf;  $103^\circ\text{C}$ ), opal-CT lepispheres in the SEM image are indicated by white arrows. Note that the lepispheres are larger ( $\sim 2\text{--}3\ \mu\text{m}$ ) and have more distinctive blades than in the shallower sample (b). The gray bar indicates the range of positions of the opal-CT characteristic diffraction peak.

detectable opal-CT and the deepest occurrence of opal-CT, is  $\sim 121\ \text{m}$  and  $\sim 173\ \text{m}$ , respectively (Table 1). However, at Site U1546, the opal-CT zone includes an intrusive sill ( $\sim 75\ \text{m}$  thick) with overlying and underlying contact zones where authigenic quartz is the main silica phase (the thickness of the contact zone is  $\sim 20\ \text{m}$  above and  $\sim 15\ \text{m}$  below the sill; Cheviet et al., 2023). The sill and the quartz-dominated contact zones divide the porcelanite host rock into two parts and limit the actual thickness of opal-CT sediment to only  $\sim 60\ \text{m}$ . The depths at which the transition from opal-CT to quartz occurs is also different

between the two sites. At Site U1546, opal-CT is first observed to be entirely converted into authigenic quartz at  $\sim 346\ \text{mbsf}$ , which is  $\sim 123\ \text{m}$  shallower than the depth at which it is first found at Site U1545 ( $\sim 469\ \text{mbsf}$ ), clearly resulting from the (hydro)thermal impact of the underlying intrusion (Teske et al., 2021; Lizarralde et al., 2023). Below the sill, the sequence of silica phases occurs in reverse, starting with quartz in the metamorphic contact aureole below the sill to the depth of  $\sim 447\ \text{mbsf}$ , and then transitioning to a reoccurrence of opal-CT below the quartz-bearing zone. Opal-CT remains the dominant silica phase to a

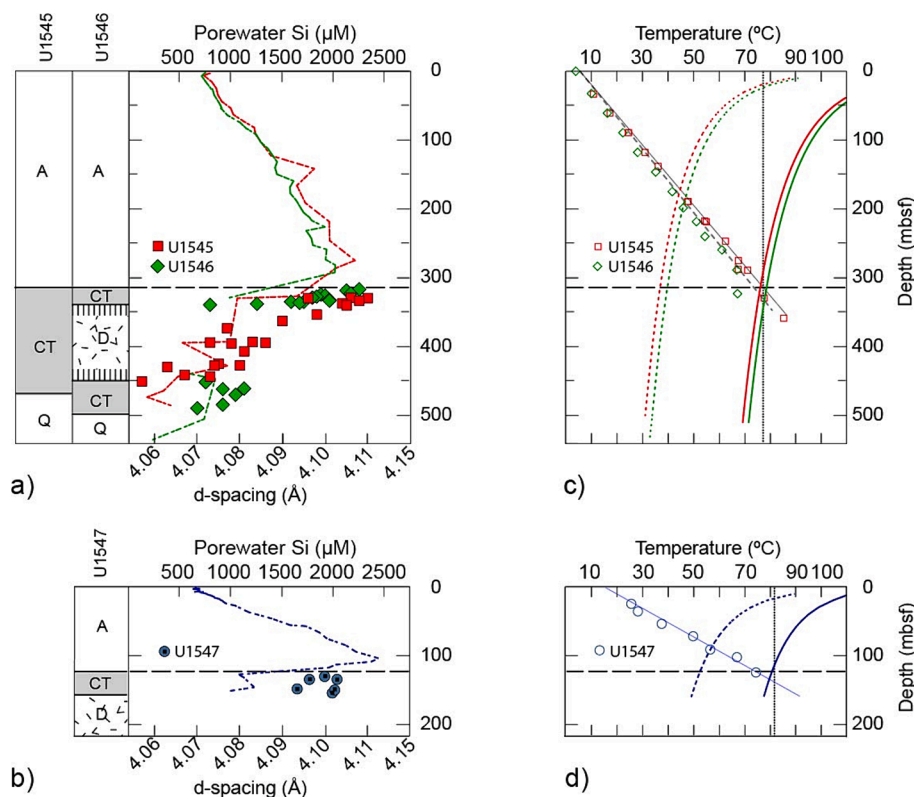


**Fig. 3.** (a, b) The columns to the left of the plots represent simplified, lithological intervals highlighting the main silica phases (A = opal-A, CT = opal-CT, Q = quartz, and intrusive dolerite bodies (D) present for each of the three sites). The vertical dashed lines show the approximate extent of the metamorphic contact aureole associated with the massive mafic sill at Site U1546. The changes in porewater silica content in  $\mu\text{M}$  (dashed curves) and the d-spacing ( $\text{\AA}$ ) of opal-CT are plotted vs. depth (mbsf) in (a) for Site U1545 (red) and Site U1546 (green), and in (b) for Site U1547 (blue). Panels (c, d) show the linear changes of in situ temperature vs. depth (mbsf) and the temperature evolution of opal-CT precipitation with depth as predicted by two kinetic models: ‘classic’ – dashed line (Mizutani, 1970), and the new kinetic model (this paper) – solid line for Sites U1545/U1546 (c) and Site U1547 (d). Note that the new kinetic model (solid lines) predicts more closely the actual depth/temperature of initial XRD-based opal-CT detection (dashed line) at the point of their intersection (vertical dotted line).

depth of  $\sim 501$  mbsf below which silica is again entirely converted into quartz (Fig. 3a).

Like the northwestern Guaymas Basin Sites U1545 and U1546, the transition from opal-A to opal-CT at Site U1547 corresponds to the lithologic change from diatom ooze to porcelanite (Fig. 3b). This occurs, however, over a significantly shallower and shorter depth interval of  $\sim 103$ – $127$  mbsf and at a comparable, yet slightly higher range of temperature (Table 1), representing a linear geothermal gradient of  $529$   $^{\circ}\text{C}/\text{km}$  (Teske et al., 2021). Biosilica dissolution increases more rapidly than at Sites U1545 and U1546 and the maximum concentration of porewater silica ( $\sim 2445$   $\mu\text{M}$ ) is reached at a relatively shallow subsurface depth ( $\sim 103$  mbsf). Opal-CT was detected by XRD at  $\sim 127$  mbsf, corresponding to an *in situ* temperature of  $\sim 77$   $^{\circ}\text{C}$ , marking the shallowest depth of porcelanite occurrence amongst the three sites studied. The opal-CT zone extends only to a depth of  $\sim 150$  mbsf right above the top contact of a mafic sill with only a few cm of intervening authigenic quartz. This massive sill body was not drilled through; thus, deeper sediment data are not available.

## 4. Discussion

### 4.1. Ordering of opal-CT with temperature

The shallow crustal sections recovered by IODP X385 at the three drill sites studied feature (1) exceptionally high sedimentation rates of mainly diatomaceous sediments (up to  $1$  m/kyr), (2) very high geothermal gradients ( $\sim 221$ – $529$   $^{\circ}\text{C}/\text{km}$ ), and (3) silica diagenesis occurring in young sediments of middle to late Pleistocene age (Teske et al., 2021). The *in situ* temperatures of biogenic to authigenic silica

transition are within a similar, narrow range at these three sites. However, at Site U1547, the change occurs at a depth that is  $\sim 2.3$  times shallower, clearly reflecting the  $\sim 2.3$  times higher geothermal gradient at this site compared to Sites U1545 and U1546 (Fig. 3; Table 1). The temperature-depth relationship for the onset of opal-CT precipitation thus suggests that the silica transformation depth correlates with the local geothermal gradient, confirming the previously reported impact of the thermal regime in other marine basins with high heat flow and rapid sediment burial (e.g., Riech and von Rad, 1979; Pisciotto, 1981).

Still, the Guaymas Basin sites are exceptional because the very high temperatures at which opal-CT is first observed are the highest ever reported from a natural system, and much ( $> \sim 20$   $^{\circ}\text{C}$ ) higher than predicted by existing kinetic models. In addition, the age of the sediments in which the silica transformation occurs is extremely young ( $\leq 0.44$  Ma). For instance, despite similar sediment lithology and relatively high geothermal gradients in the Sea of Japan back-arc basin (Iijima and Tada, 1981; Ingle et al., 1990; Langseth and Tamaki, 1992; Pisciotto et al., 1992) and in the Bering Sea (Hein et al., 1978), opal-CT precipitates within a lower range of temperatures ( $\sim 20$ – $51$   $^{\circ}\text{C}$ ) and in older sediments (Table 4). Although the range of temperatures in which the ordering of opal-CT occurs is higher than previously reported, the range of opal-CT d-spacing values measured at the IODP X385 sites (between  $\sim 4.11$  and  $\sim 4.05$   $\text{\AA}$ ) is identical to the values previously reported in the literature for the diagenetic silica trends of opal-CT in the Monterey Formation in the Temblor Range and in Santa Maria Valley (Murata and Larson, 1975; Pisciotto, 1981) and in cores from northern Japan (Iijima and Tada, 1981; Kano, 1983).

At Sites U1545 and U1546, the opal-A to opal-CT silica transformation front, which is defined as the initial depth of XRD-detectable

opal-CT in the sediments, occurs within a narrow range of *in situ* temperatures (between ~74 and 79 °C; Table 1). Opal-CT (101) peak d-spacing values for the shallowest opal-CT samples are similar amongst the two sites (~4.10 Å), thus irrespective of the presence and/or depth of the sill intrusion at Site U1546. However, while d-spacing decreases linearly with depth at Site U1545, reflecting increased ordering throughout the opal-CT zone, the ordering trend is interrupted by the sill at adjacent Site U1546 (Fig. 2a). Notably, in the opal-CT zone above the sill, d-spacing decreases more steeply than at Site U1545, reflecting the thermal overprint from the underlying sill intrusion. Hence, the location of the opal-A to opal-CT silica transformation front is primarily the product of burial diagenesis and the local geothermal gradient, whereas the sill influences silica diagenesis mainly within the thermal overprint zone of the intrusion. In a contrasting interpretation of results obtained from the on-axis drill sites of DSDP Leg 64, opal-CT formation in sediments sandwiched between stacked intrusive bodies was explained as a consequence of trapping silica-rich hydrothermal fluids (Kastner and Siever, 1983).

Since the sedimentary column at Site U1545 is not crosscut by a thick sill, the gradual ordering of opal-CT in relation to depth and temperature at this site is mainly the result of burial diagenesis. Hence, opal-CT d-spacing can be interpreted as being in equilibrium with the *in situ* temperature. The relationship between d-spacing ( $d(\text{Å})$ ) and temperature ( $T$ ) is significantly linear ( $p = 1.43 \times 10^{-9}$ ) and the strength of the linear regression model is supported by the distribution of the residuals which is unbiased and homoscedastic (Fig. 4).

$$T(^{\circ}\text{C}) = -577.47 \times d(\text{Å}) + 2451.3 \quad R^2 = 0.861 \quad (n = 21) \quad (1)$$

The model provides a crystallographic tool to estimate the maximum temperature conditions for the opal-CT sediments located above the sill at Site U1546 (Table 3). The delta between the maximum temperature based on d-spacing (Eq. (1)) and the *in situ* temperature increases downhole and is largest for the sample closest to the top of the sill, reflecting (hydro)thermal overprint.

The hydrothermal experiments by Mizutani (1977) and the isotopic evidence of Murata et al. (1977) suggest that the rate of change of opal-

CT d-spacing with depth is a temperature-dependent process which is reflective of solid–solid transition (e.g., Hein et al., 1978). However, Williams et al. (1985) observed that the peak-sharpening/shift of opal-CT observed with burial depth on XRD spectra, the loss of tridymite, and the gradual increase in opal-CT crystal size could rather suggest a dissolution-reprecipitation mechanism.

#### 4.2. Fast burial, slow kinetics

The rate of ordering of opal-CT with temperature at Site U1545 (~0.0015 Å/°C) is remarkably similar to the rate reported by Iijima and Tada (1981; see their Fig. 10) for Neogene biosiliceous sediment cores in northern Japan. Yet, the ordering of opal-CT at Site U1545 occurs within a much higher range of temperatures (~75–110 °C) than the temperature range reported for the northern Japan cores (~20–70 °C). While higher opal-A to opal-CT transition temperatures are expected for biosiliceous basins with rapid sediment burial and high heat flow (Mizutani, 1970; Pisciotto, 1981), the persistence of amorphous opaline diatom tests in the Guaymas Basin at temperatures in excess of ~70 °C challenges our current understanding of the physical conditions and the kinetic factors controlling the conversion of amorphous biosilica to opal-CT. A clue to the cause of silica transformation occurring at such high temperatures and in such young sediments in the Guaymas Basin is provided by the observation that this basin mainly differs from other Neogene basins in terms of sedimentation rates. For instance, the sedimentation rate in the Sea of Japan varies from ~45 to 175 m/Myr (Ingle et al., 1990), thus, being about one order of magnitude slower than the ~1000 m/Myr of the Guaymas Basin. Embedded in a similar but fossil marginal rift and associated geothermal setting (modern gradient of ~121–178 °C/km), the Sea of Japan sediments undergo opal-CT crystallization at lower temperatures of ~22–56 °C and at much older ages due to the slower burial (Pisciotto et al., 1992; Table 4) compared to the Guaymas Basin. Mizutani (1970) demonstrated in the laboratory setting that the time factor is a critical component for silica phase transformations. The latter author pointed out that the application of his kinetic model to silica diagenesis in natural sediments results in much longer calculated reaction times relative to those obtained in the presence of alkaline solutions used to catalyze the diagenetic reactions in his experiments. Based on this observation, Mizutani (1970) predicted that opal-CT would start precipitating after ~50 kyr at a temperature of ~50 °C in a natural system.

A clue to the potential cause of the high-temperature silica transformation in the Guaymas Basin is provided by the observation that it mainly differs from other biosiliceous depositional settings by having remarkably higher sedimentation rates (~10<sup>-3</sup>–10<sup>-4</sup> m/year), which typically range on the order of 10<sup>-6</sup> to 10<sup>-3</sup> m/year in the deep sea (Seibold and Berger, 2017). We hypothesize that biosiliceous sediments buried under conditions of both very fast sedimentation and high geothermal gradients do not experience shallow/early diagenetic transformation as previously thought (Pisciotto, 1981). Rather, the rapid burial “outpaces” the high thermal gradient resulting in the effective slowing of the kinetic reactions which are better predicted by the new kinetic parameters presented in this paper.

The opal-A to opal-CT transformation has been interpreted as a first-order kinetic reaction in which temperature affects the timing of opal-CT precipitation exponentially, and the rate constant ( $k$ ) is thermally dependent following Arrhenius' Law (Hesse and Schacht, 2011). Applying widely accepted published kinetic parameters (Mizutani, 1970) to the Guaymas Basin, Sea of Japan, and Bering Sea sites (Table 4), the predicted temperature for opal-CT occurrence is 32 °C/25 °C lower than the actual *in situ* temperature found at Sites U1545/U1546 (Fig. 3c) and 24 °C lower than at Site U1547 (Fig. 3d). However, this discrepancy is reconciled when new kinetic parameters are calculated based on the *in situ* temperature and time of precipitation of opal-CT at the Guaymas Basin, Sea of Japan, and Bering Sea sites collectively. Assuming that the precipitation of opal-CT is a first-order kinetic

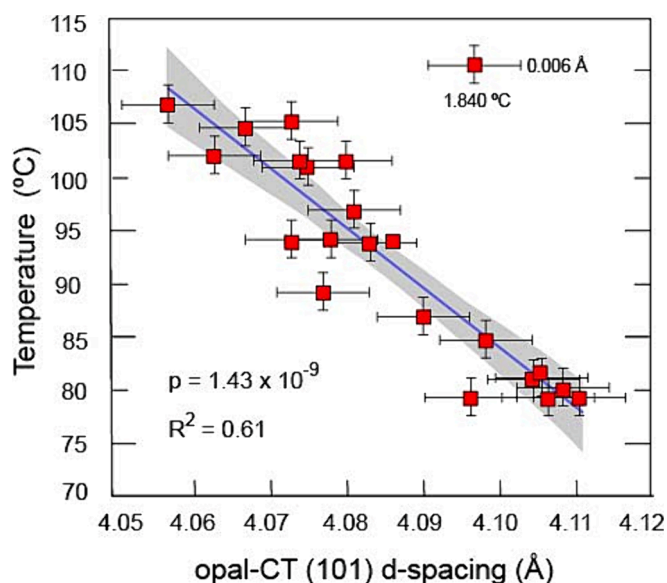


**Fig. 4.** Opal-CT d-spacing  $d(\text{Å})$  paleothermometry: the d-spacing of the opal-CT peak is plotted vs. *in situ* temperature (°C) for Site U1545 (red). The dark blue line shows the correlation between the two parameters for Site U1545, which is statistically linear (see Eq. (1) in the main text), the gray bands indicate the 95 % confidence intervals. The error bars for d-spacing and temperature are 0.006 Å and 1.840 °C, respectively. The linear correlation is highly significant and can be used as a local paleothermometer in the ~72–112 °C temperature range.

**Table 3**

Max temperatures for opal-CT samples above the sill intrusion at Site U1546 based on Site U1545 opal-CT d-spacing paleothermometry.

Sample (Hole/Core/Section/Interval)	In situ temp. (°C/km)	Depth (mbsf)	Distance from sill top	Opal-CTd-spacing (Å)	Calculated max temp. (°C/km)*	Temperature differential (calculated-in situ) (°C/km)
A_57X_4W_121-123	73.54	316.81	37.79	4.108	79.05	5.51
A_58X_1W_100-102	73.92	318.51	36.09	4.105	80.79	6.87
A_59X_1W_100-102	74.91	323.01	31.59	4.106	80.21	5.30
A_59X_2W_101-103	75.24	324.52	30.08	4.099	84.25	9.01
A_59X_3W_101-103.	75.57	326.02	28.58	4.1	83.67	8.10
A_59X_4W_102-104	75.9	327.51	27.09	4.098	84.83	8.93
A_59X_5W_102-104	76.23	329.01	25.59	4.097	85.41	9.18
A_60X_1W_120-122	76.89	332.01	22.59	4.101	83.10	6.21
A_60X_2W_120-122	77.22	333.51	21.09	4.101	83.10	5.88
A_60X_3W_121-123	77.55	335.02	19.58	4.092	88.29	10.74
A_60X_3W_131-141	77.583	335.15	19.45	4.095	86.56	8.98
A_60X_4W_120-122	77.88	336.51	18.09	4.094	87.14	9.26
A_60X_5W_119-121	78.21	338.01	16.59	4.084	92.91	14.70
A_60X_6W_119-121	78.54	339.51	15.09	4.073	99.26	20.72

Notes: GB = at Site U1546 the intrusive sill occurs between ~354.6 and 430.0 mbsf; \*calculation made based on the Site U1545 silica paleothermometer (see Eq. (1)).

**Table 4**

Temperatures, depths, ages and kinetic model predictions for opal-CT precipitation.

Location	Leg/Exp.	Site	Temp. (°C/km)	Temp. (°C/Myr)	Sed. rate (mm/yr)	Opal-A/CT (mbsf)	Opal-A/CT (Ma)	Opal-A/CT (°C)	Kinetic Model Results				
									*Rate constant k	‡Temp. (C°)	§Temp. (C°)	‡Time (Ma)	§Time (Ma)
GB	385	U1545	225	194.18	0.86	329	0.38	79	2.764E-07	47	76	0.24	0.39
GB	385	U1546	221	225.42	1.02	317	0.31	74	3.390E-07	49	78	0.22	0.35
GB	385	U1547	529	277.2	0.52	127	0.24	77	4.347E-07	53	82	0.20	0.31
JS	127	794	118	4.37	0.04	293	7.90	37	1.334E-08	12	39	2.82	8.98
JS	127	795	132	7.00	0.05	325	5.20	44	2.026E-08	17	44	2.38	6.26
JS	127	796	178	7.39	0.04	215	6.00	43	1.756E-08	15	42	2.05	5.71
JS	127	797	121	3.69	0.03	299	8.00	36	1.317E-08	12	39	3.30	10.58
JS	128	798	117	14.16	0.12	455	3.76	51	2.802E-08	20	47	1.42	3.35
JS	128	799	95	6.65	0.07	450	6.43	46	1.639E-08	14	41	2.17	6.23
BE	19	184	82	70.77	0.13	600	4.62	35	2.283E-08	18	45	0.25	0.64

Notes: GB = Guaymas Basin, IODP Expedition 385 (this paper); JS = Japan Sea, ODP Legs 127 and 128; BE = Bering Sea, DSDP Leg 19. \*All first occurrences of opal-CT are for opal-CT/opal-A=0.11. The Arrhenius equation [ $k=A^\circ \exp(-E_a/RT)$ ] used the following kinetic parameters: gas constant  $R=8.314$  (J/mol); ‡Mizutani's (1970) kinetic model,  $E_a=-66944$  (J/mol),  $A^\circ=2.37E+4$  (years<sup>-1</sup>); § this paper's kinetic model,  $E_a=-70031$  (J/mol),  $A^\circ=8421$  (years<sup>-1</sup>).

reaction, the reaction rate constant (k) is

$$k = -\ln(1 - C_{CT}(t))/t \quad (2)$$

where  $C_{CT}(t)$  is the concentration of opal-CT at the time t. Using the age of the sample in which opal-CT was first detected by XRD and assuming that opal-CT/opal-A = 0.11, the reaction rate constant k can be calculated using ( $k = -\ln(0.9)/t$ ) for each site (Table 4). The reaction rate constant k is thermally dependent and follows the Arrhenius equation:

$$k = Ae^{-E_a/RT} \quad (3)$$

where R is the gas constant, T is the temperature (K), and the kinetic parameters A and  $E_a$  are the frequency factor and the activation energy, respectively. The Arrhenius equation can be transformed into

$$\ln(k) = \ln(A) - E_a/RT \quad (4)$$

Eq. (4) can be fit with the general linear equation

$$y = -(E_a/R) \cdot 1/x + \ln(A) \quad (5)$$

where  $\ln(k)$  is a function of  $1/T$ , and the kinetic parameters A and  $E_a$  can be calculated using a best fit function ( $E_a = -70031$  (J/mol),  $A = 8421$  (a<sup>-1</sup>); Table 4). Because of the relatively low number of sites included in the calculation the statistical results obtained for the Arrhenius parameters calculation presented in this paper should be taken with caution ( $R^2 = 0.93$ ,  $n = 10$ ,  $p = 6.7 \times 10^{-6}$ ; Fig. S1). Nevertheless, the temperatures predicted using the newly calculated kinetic parameters are

much closer to the empirical data for all deep-sea sites considered (Fig. 3c/d; Table 4). Importantly, the new kinetic parameters account for much slower reaction times not only at the Guaymas Basin sites but also in other fast accumulation settings, compared to other deep-sea sites, thus, suggesting that factors intrinsic to the geologic settings of these basins (e.g., extremely high burial rates of biosilica) could be responsible for the attenuated rates of silica transformation.

To test the hypothesis that rapid burial and accumulation of biosiliceous sediments in areas with high geothermal gradients impedes their diagenetic reactivity, we calculated the depth/temperature dependence of opal-CT precipitation with previously published kinetic parameters (Mizutani, 1970) but using reaction constant k values that reflect slower sedimentation rates. The latter was simulated by reducing the time factor (t) in  $k = -\ln(0.9)/t$  to a value between 0.1 and 0.2. The best fit between previous kinetic parameters and the new kinetic model (which in turn best predicts the empirical data) was obtained when sedimentation rates are reduced by a factor of 0.14 (Fig. S2; Table S4). In other words, the 'classic' kinetic model (Mizutani, 1970) for silica diagenesis best fits the empirical data from IODP X385 when the sedimentation rates are simulated to be about one order of magnitude lower than in the Guaymas Basin. This test does not demonstrate directly that rapid burial in the Guaymas Basin is responsible for protectively shuttling amorphous silica through temperatures that are much higher than the previously known stability field for opal-A (~18–56 °C). However, it does provide evidence that if the Guaymas Basin had sedimentation/burial rates like biosiliceous basins elsewhere, the kinetic models that have been applied to a variety of other deep-sea, geological, and

laboratory settings would work for this basin as well.

#### 4.3. Potential role of solution chemistry

The time and depth of the opal-A to opal-CT transition may also be influenced by the chemical composition and silica saturation state of the solution from which authigenic silica precipitates. The Guaymas Basin IODP X385 sites are lithologically similar to the well-studied diatomite-dominated Monterey Formation (Kastner et al., 1977; Keller and Isaacs, 1985) and to other biosiliceous deposits in which opal-CT precipitation occurs at much lower *in situ* temperatures (e.g., Pisciotto, 1981; Bohrmann et al., 1994). Even though temperature exerts the main control on silica phase change, previous studies have shown that lithology and solution chemistry can also affect the timing of the transition from opal-A to opal-CT (Kastner et al., 1977; Keller and Isaacs, 1985). The presence of metal hydroxides (commonly used for silica precipitation in industrial applications; Iler, 1955) is thought to be instrumental in the nucleation of opal-CT. Thus, cation removal from solution in siliceous sediments rich in clay minerals (e.g., Mg<sup>2+</sup> compatible in smectite) requires temperature increases (by ~2–5 °C) for opal-CT precipitation (Kastner, 1977; Keller and Isaacs, 1985). Therefore, the presence of subordinate sedimentary components, such as dissolved or solid organic matter, or the removal of dissolved Mg from porewater by formation of authigenic clay minerals (e.g., smectite; Keller and Isaacs, 1985) or dolomite (which is present at all three sites studied; Teske et al., 2021), could have retarded opal-CT precipitation. However, even an increase of 5 °C due to cation removal would not account for the > 20 °C difference between the highest temperatures for opal-CT previously reported in the literature (56 °C) and the temperature at which the precipitation initiates in Guaymas Basin (~79 °C). Also, the IODP X385 sites do not show marked trends in the relative abundance of clay minerals versus the biosiliceous fraction in relation to the depth at which the initial opal-CT precipitation is observed. Nevertheless, instead of clay minerals, carbonates may form the major sink for Mg in the Guaymas Basin, as the stratigraphic interval above the opal-A/opal-CT boundary at all three sites is characterized by the occurrence of micrite mainly composed of dolomite [CaMg(CO<sub>3</sub>)<sub>2</sub>] (Teske et al., 2021).

One implication of our kinetic models is that the opal-A/opal-CT transition may not be simply treated as first-order chemical reaction in subsurface regions characterized by rapid burial and high geothermal gradients. Instead, the effects of temperature reactions on silica phase change could rather be inhibited by the stability of the metastable phases. During advancing sediment burial in closed systems, the increasing pore water silica concentrations may reach supersaturation with respect to opal-A before the complete dissolution of opal-A has occurred. As a consequence, opal-A, the thermodynamically least stable phase persists (Fig. 3). The saturation state with respect to silica in the porewater, calculated using temperature-dependent solubility equations by Gunnarsson and Arnórsson (2000), is described by the depth distributions of the saturation indexes (SI) displayed in Fig. S3. Throughout the opal-A zones at all three IODP X385 sites, the solution is near saturation with respect to opal-A. However, while opal-CT is above saturation, this phase does not precipitate. Thus, the transition from opal-A to opal-CT might be inhibited as long as the more metastable phase (opal-A) remains supersaturated (Ostwald's step rule; e.g. Meister et al., 2014). It is only when the porewater silica concentrations are below saturation for opal-A (opal-CT) that the more stable opal-CT (quartz) phase begins to precipitate (Fig. S3). The distribution of the saturation indexes for opal-CT in its corresponding zone of occurrence also shows that the porewater concentration of silica is at its lower limit with respect to opal-CT saturation suggesting that the transformation from opal-A to opal-CT could be limited by the dissolution rate of opal-A rather than the nucleation and growth of opal-CT (Meister et al., 2022).

In summary, while the solution chemistry and the presence of other lithologies (e.g. clay minerals, dolomite) do not seem to play a significant role, the saturation state of the porewater silica concentrations with

respect to opal-A could be an additional factor causing opal-CT precipitation at much higher temperatures than previous models have predicted. Hence, the rapid increase in temperature in the subsurface of the Guaymas Basin has two major contrasting effects on the thermochemical processes that control silica diagenesis. On the one hand, it accelerates the kinetics of the reaction as shown by early experimental data (e.g., Mizutani, 1970). On the other hand, a quickly increasing temperature due to a comparatively high geothermal gradient increases the solubility of silica and inhibits the precipitation of the more thermodynamically stable phases opal-CT as long as the metastable phases opal-A remains supersaturated (Ostwald's step rule).

## 5. Conclusions

New mineralogic data combined with *in situ* downhole temperature measurements obtained from deep-sea biosiliceous sediments cored in the off-axis subsurface region of the Guaymas Basin (IODP X385, Gulf of California, Mexico) provide an unprecedented insight into the mineralogic transformations of biosilica in a basin where both geothermal gradients and sedimentation rates are exceptionally high. Despite the extremely hot subsurface environment and the presence of an extensive network of igneous sills, the transformation from opal-A to opal-CT occurs at much higher *in situ* temperatures (~74–79 °C) than ever reported, and in older/deeper sediments than current kinetic models would have predicted.

The depth range of the Guaymas Basin opal-A to opal-CT silica transformation front is primarily the product of the local geothermal gradient while the impact of sill intrusion on silica diagenesis occurs mainly within a relatively narrow zone of thermal overprint. At Site U1545, where there is no evidence of contact metamorphic overprint due to sill intrusion, the ordering of opal-CT correlates with temperature, thus, enabling the establishment of a predictive relationship between silica diagenetic maturity and *in situ* temperature for this basin (over the range of ~72–112 °C). The silica paleothermometer was applied to the nearby Site U1546 to calculate both the maximum temperature and the extent of the thermal overprint on the opal-CT sediments above a cross-cutting sill.

The kinetics of silica transformation in the Guaymas Basin can be better predicted using new, empirically founded kinetic parameters that account for slower rates of silica transformation based on this study and available data sets from similar biosiliceous basins. We conclude that the apparent 'sluggishness' of silica transformation in basins with sediments produced by biosiliceous upwelling, such as the Guaymas Basin, reflects the limitation of previously established kinetic models to predict the evolution of silica diagenesis in settings where burial rates are much faster than those typical of biogenic sedimentation in the open ocean. Therefore, this novel perspective on the reaction of silica phase change is expected to enable a more reliable modelling of sedimentary evolution in biosiliceous upwelling basins in general.

## Data availability

Data are available through EarthChem Library at <https://doi.org/10.26022/IEDA/112954>.

## CRedit authorship contribution statement

**Ivano W. Aiello:** Writing – review & editing, Writing – original draft, Methodology, Investigation, Funding acquisition, Formal analysis, Conceptualization. **Tobias W. Höfing:** Writing – review & editing, Writing – original draft. **Armelle Riboulleau:** Writing – review & editing, Writing – original draft. **Andreas P. Teske:** Writing – review & editing. **Daniel Lizarralde:** Writing – review & editing. **Jeanine L. Ash:** Writing – review & editing. **Diana P. Bojanova:** Writing – review & editing. **Martine D. Buatier:** Writing – review & editing. **Virginia P. Edgcomb:** Writing – review & editing. **Christophe Y. Galerne:** Writing

– review & editing. **Swanne Gontharet**: Writing – review & editing. **Verena B. Heuer**: Writing – review & editing. **Shijun Jiang**: Writing – review & editing. **Myriam A.C. Kars**: Writing – review & editing. **Ji-Hoon Kim**: Writing – review & editing. **Louise M.T. Koornneef**: Writing – review & editing. **Kathleen M. Marsaglia**: Writing – review & editing. **Nicolette R. Meyer**: Writing – review & editing. **Yuki Morono**: Writing – review & editing. **Raquel Negrete-Aranda**: Writing – review & editing. **Florian Neumann**: Writing – review & editing. **Lucie C. Pastor**: Writing – review & editing. **Manet E. Peña-Salinas**: Writing – review & editing. **Ligia L. Pérez-Cruz**: Writing – review & editing. **Lihua Ran**: Writing – review & editing. **John A. Sarao**: Writing – review & editing. **Florian Schubert**: Writing – review & editing. **S. Khogenkumar Singh**: Writing – review & editing. **Joann M. Stock**: Writing – review & editing. **Laurent Toffin**: Writing – review & editing. **Wei Xie**: Writing – review & editing. **Toshiro Yamanaka**: Writing – review & editing. **Guangchao Zhuang**: Writing – review & editing.

### Declaration of competing interest

The authors declare that they have no known competing financial interests or personal relationships that could have appeared to influence the work reported in this paper.

### Acknowledgments

We sincerely thank the IODP technical staff and the R/V *JOIDES Resolution* crew of Expedition 385 for their invaluable assistance. I.W.A. was supported by National Science Foundation (NSF) award no. MRI-1827628. T.W.H. acknowledges support from NSF award no. OCE-1326927. A.T. was supported by the U.S. Science Support Program (NSF-OCE 1450528). I.W.A.: U.S. Science Support Program (NSF-OCE 1450528). The authors are also very grateful to Dr. Sophie Westacott and two anonymous reviewers for their valuable comments and suggestions, which greatly improved the manuscript.

### Appendix A. Supplementary material

Supplementary material to this article can be found online at <http://doi.org/10.1016/j.gca.2024.07.005>.

### References

- Aiello, I.W., Garrison, R.E., Moore, J.C., Kastner, M., Stakes, D.S., 2001. Anatomy and origin of carbonate structures in a Miocene cold-seep field. *Geology* 29, 1111–1114.
- Baumgartner, T., Ferreira-Bartrina, V., Schrader, H., Soutar, A., 1985. A 20-year varve record of siliceous phytoplankton variability in the central Gulf of California. *Marine Geology*, 64, 113–129.
- Bohrmann, G., Abelmann, A., Gersonde, R., Hubberten, H., Kuhn, G., 1994. Pure siliceous ooze, a diagenetic environment for early chert formation. *Geology* 22, 207–210.
- Calvert, S.E., 1966. Accumulation of Diatomaceous Silica in the Sediments of the Gulf of California. *Geol. Soc. Am. Bull.* 77, 569–596.
- Chaika, C., Dvorkin, J., 2000. Porosity reduction during diagenesis of diatomaceous rocks. *Am. Ass. of Petr. Geol. Bull.* 84, 1173–1184.
- Cheviet, A., Buatier, M., Choulet, F., Galerne, C., Ribouilleau, A., Aiello, I., Marsaglia, K. M., Höfig, T.W., 2023. Contact metamorphic reactions and fluid–rock interactions related to magmatic sill intrusion in the Guaymas Basin. *Eur. J. Mineral.* 35, 987–1007.
- Davies, R.J., Goulet, N.R., Meadows, D., 2008. Fluid flow due to the advance of basin-scale silica reaction zones. *Geol. Soc. Am. Bull.* 120, 195–206.
- Douglas, R., Gonzalez-Yajimovich, O., Ledesma-Vazquez, J., Staines-Urias, F., 2007. Climate forcing, primary production and the distribution of Holocene biogenic sediments in the Gulf of California. *Quatern. Sci. Rev.* 26, 115–129.
- Einsele, G., Gieskes, J.M., Curray, J., Moore, D.M., Aguayo, E., Aubry, M.P., Fornari, D., Guerrero, J., Kastner, M., Kelts, K., Lyle, M., 1980. Intrusion of basaltic sills into highly porous sediments, and resulting hydrothermal activity. *Nature* 283, 441–445.
- Elzea, J.M., Odom, I.E., Miles, W.J., 1994. Distinguishing well ordered opal-CT and opal-C from high temperature cristobalite by X-ray diffraction. *Anal. Chim. Acta.* 286, 107–116.
- Folk, R.L., McBride, E.F., 1978. Radiolarites and their relations to subjacent ‘oceanic crust’ in Liguria. *Italy. J. of Sed. Petr.* 48, 069–1102.
- Gross, M.R., 1995. Fracture partitioning: Failure mode as a function of lithology in the Monterey Formation of coastal California. *Geol. Soc. Am. Bull.* 107, 779–792.

- Gunnarsson, I., Arnórsson, S., 2000. Amorphous silica solubility and the thermodynamic properties of H4SiO4 in the range of 0 to 350 C at Psat. *Geochimica Et Cosmochimica Acta* 64 (13), 2295–2307.
- Heath, G.R., 1974. Dissolved silica in deep-sea sediments. In: Hay, W.W. (Ed.), *Studies in paleo-oceanography*. Soc. Econ. Paleo. Min. Spec. Publ., Tulsa, OK, 20, pp.77–93.
- Hein, J.R., Karl, S.M., 1983. Comparisons between open-ocean and continental margin chert sequences. In: *Developments in Sedimentology*, vol. 36, Elsevier, pp. 25–43.
- Hein, J.R., Scholl, D.W., Barron, J.A., Jones, M.G., Miller, J., 1978. Diagenesis of late Cenozoic diatomaceous deposits and formation of the bottom simulating reflector in the southern Bering Sea. *Sedimentology*, 25, 155–181.
- Herdianita, N.R., Rodgers, K.A., Browne, P.R., 2000. Routine instrumental procedures to characterise the mineralogy of modern and ancient silica sinters. *Geothermics*, 29, 65–81.
- Hesse, R., Schacht, U., 2011. Early diagenesis of deep-sea sediments, in: *Developments in Sedimentology*, vol. 63, Elsevier, pp. 557–713.
- Iijima, A., Tada, R., 1981. Silica diagenesis of Neogene diatomaceous and volcanoclastic sediments in northern Japan. *Sedimentology* 28, 185–200.
- Iler, R.K., 1955. *The colloidal chemistry of silica and silicates*. Cornell University Press, New York.
- Ingle, J.C., Jr., Suyehiro, K., von Breyman, M.T., 1990. *Proc. ODP, Init. Repts.*, 128, College Station, TX (ODP).
- Ingle, J.C., 1981. Origin of Neogene diatomites around the north Pacific rim. In: Garrison, R.E., Douglas, R.G. (Eds.), *The Monterey Formation and Related Siliceous Rocks of California*, Society of Economic Paleontologists and Mineralogists, vol. 20, Pac. Sec., Spec. Pub., Los Angeles, pp. 159–179.
- Isaacs, C.M., 1981. Porosity reduction during diagenesis of the Monterey Formation, Santa Barbara coastal area, California. In: Garrison, R.E., Douglas, R.G. (Eds.), *The Monterey Formation and Related Siliceous Rocks of California*, vol. 20, Soc. Econ. Paleo. Min. Spec. Publ., Pac. Sec., Los Angeles, pp. 257–271.
- Jones, J.T., Segnit, E.R., 1971. The nature of opal I. Nomenclature and constituent phases. *J. Geol. Soc. Australia* 18, 57–68.
- Kano, K., 1983. Ordering of opal-CT in diagenesis. *Geochem. J.* 17, 87–93.
- Kastner, M., 1981. Authigenic silicates in deep-sea sediments: formation and diagenesis. *The Sea* 7, 915–980.
- Kastner, M., Siever, R., 1983. Siliceous sediments of the Guaymas Basin: the effect of high thermal gradients on diagenesis. *J. Geol.* 91, 629–641.
- Kastner, M., Keene, J.B., Gieskes, J.M., 1977. Diagenesis of siliceous oozes—I. Chemical controls on the rate of opal-A to opal-CT transformation—an experimental study. *Geochim. Cosmochim. Acta* 41, 1041–1059.
- Keller, M.A., Isaacs, C.M., 1985. An evaluation of temperature scales for silica diagenesis in diatomaceous sequence including a new approach based on the Miocene Monterey Formation. *California. Geo-Mar. Lett.* 5, 31–35.
- Kuramoto, S., Tamaki, K., Langseth, M.G., Nobes, D.C., Tokuyama, H., Pisciotto, K.A., Taira, A., 1992. 73. Can opal-A/opal-CT BSR be an indicator of the thermal structure of the Yamato Basin, Japan Sea. *Age* 794, 36.
- Lancelot, Y., 1973. Chert and silica diagenesis in sediments from the Central Pacific. In: Winterer, E.L., Ewing, J.I. (Eds.), *Initial Reports of the Deep Sea Drilling Project 17*. Government Printing Office, Washington, U.S., pp. 377–405.
- Langseth, M.G., Tamaki, K., 1992. Geothermal measurements: thermal evolution of the Japan Sea basins and sediments. In: Tamaki, K., Suyehiro, K., Allan, J., McWilliams, M., (Eds.), *Proc. ODP, Sci. Results*, 127/128 (Pt. 2), College Station, TX (ODP), pp. 1297–1309.
- Liesegang, M., Tomaschek, F., 2020. Tracing the continental diagenetic loop of the opal-A to opal-CT transformation with X-ray diffraction. *Sed. Geol.* 398, 105603.
- Lizarralde, D., Axen, G.J., Brown, H.E., Fletcher, J.M., González-Fernández, A., Harding, A.J., Holbrook, W.S., Kent, G.M., Paramo, P., Sutherland, F., Umhoefer, P. J., 2007. Variation in styles of rifting in the Gulf of California. *Nature* 448, 466–469.
- Lizarralde, D., Soule, S.A., Seewald, J.S., Proskurowski, G., 2011. Carbon release by off-axis magmatism in a young sedimented spreading centre. *Nat. Geosci.* 4, 50–54.
- Lizarralde, D., Teske, A., Höfig, T.W., González-Fernández, A., IODP Expedition, 385 Scientists, 2023. Carbon released by sill intrusion into young sediments measured through scientific drilling. *Geology* 51, 329–333.
- Meister, P., Chaplignin, B., Picard, A., Meyer, H., Fischer, C., Rettenwander, D., Amthauer, G., Vogt, C., Aiello, I.W., 2014. Early diagenetic quartz formation at a deep iron oxidation front in the Eastern Equatorial Pacific. *Geochim. Cosmochim. Acta* 137, 188–207.
- Meister, P., Herda, G., Petrishcheva, E., Gier, S., Dickens, J., Liu, B., 2022. Microbial alkalinity production and silicate alteration in methane charged marine sediments: implications for porewater chemistry and diagenetic carbonate formation. *Front. Earth Sci.* 9 (756591), 1–18.
- Mizutani, S., 1970. Silica minerals in the early stage of diagenesis. *Sedimentology*, 15, 419–436.
- Mizutani, S., 1977. Progressive ordering of cristobalitic silica in the early stage of diagenesis. *Contributions Mineral. Petrol.* 61 (2), 129–140.
- Murata, K.J., Larson, R.R., 1975. Diagenesis of Miocene siliceous shales, Temblor range, California. *USGS J. Res.* 3, 553–566.
- Neumann, F., Negrete-Aranda, R., Harris, R.N., Contreras, J., Galerne, C.Y., Peña-Salinas, M.S., Spelz, R.M., Teske, A., Lizarralde, D., Höfig, T.W., Expedition 385 Scientists, 2023. Heat flow and thermal regime in the Guaymas Basin, Gulf of California: estimates of conductive and advective heat transport. *Basin Research* 00, 1–21.
- Pisciotto, K.A., 1981. Distribution, thermal histories, isotopic compositions, and reflection characteristics of siliceous rocks recovered by the Deep Sea Drilling Project. *Society of Econ. Paleo. and Mineral Spec. Pub.* 32, 129–147.
- Pisciotto, K.A., Garrison, R.E., 1981. Lithofacies and depositional environment of the Monterey Formation, California. In: Garrison, R.E., Douglas, R.G. (Eds.), *The*

- Monterey Formation and Related Siliceous Rocks of California, Soc. Econ. Paleo. Min. Spec. Publ., Pacific Section, Los Angeles, 20, pp. 97-122.
- Pisciotta, K.A., Murray, R.W., Brumsack, H.J., 1992. 3. Thermal history of Japan Sea sediments from isotopic studies of diagenetic silica and associated pore waters. In: Proc. ODP, Sci. Results, 127/128 (Pt. 1), Pisciotta, K.A., Ingle, J.C., Jr., von Breymann, M.T., Barron, J. (Eds.), College Station, TX, pp. 49-46.
- Riech, V., von Rad, U., 1979. Silica diagenesis in the Atlantic Ocean: diagenetic potential and transformations. Deep Drilling Results in the Atlantic Ocean: Continental Margins and Paleoenvironment. 3, 315–340.
- Seibold, E., Berger, W., 2017. The sea floor: an introduction to marine geology. Springer.
- Teske, A., Lizarralde, D., Höfig, T.W., and the Expedition 385 Scientists, 2021. Guaymas Basin Tectonics and Biosphere. Proc. of the IODP, 385, College Station, TX.
- Teske, A., McKay, L.J., Ravelo, A.C., Aiello, I., Mortera, C., Núñez-Useche, F., Canet, C., Chanton, J.P., Brunner, B., Hensen, C., Ramírez, G.A., Sibert, R.J., Turner, T., White, D., Chambers, C.R., Buckley, A., Joye, S.B., Soule, S.A., Lizarralde, D., 2019. Characteristics and evolution of sill-driven off-axis hydrothermalism in Guaymas Basin—the Ringvent site. *Scient. Rep.* 9, 13847.
- Thunell, R.C., Pride, C., Tappa, E., Muller-Karger, F., 1993. Varve formation in the Gulf of California: Insights from time series sediment trap and remote sensing. *Quat. Sci. Rev.* 12, 451–464.
- Tréguer, P.J., De La Rocha, C.L., 2013. The world ocean silica cycle. *Ann. Rev. Mar. Sci.* 5, 477–501.
- Williams, L.A., Crerar, D.A., 1985. Silica diagenesis II. General Mechanisms. *J. Sediment. Petrol.* 55, 312–321.
- Williams, L.A., Parks, G.A., Crerar, D.A., 1985. Silica diagenesis; I. Solubility controls. *J. Sediment. Petrol.* 55, 301–311.